Cohesive Modeling of Dynamic Crack Growth in Homogeneous and Functionally Graded Materials

Zhengyu Zhang[a], Glaucio H. Paulino[a] and Waldemar Celes[b]

[a]*Department of Civil and Environmental Engineering, University of Illinois at Urbana-Champaign, Newmark Laboratory, 205 North Mathews Avenue, Urbana, IL 61801, U.S.A.*
[b]*Tecgraf/PUC-Rio Computer Science Department, Pontifical Catholic University of Rio de Janeiro, Rua Marquês de São Vicente 225, Rio de Janeiro, RJ, 22450-900, Brazil*

Abstract. This paper presents a Cohesive Zone Model (CZM) approach for investigating dynamic crack propagation in homogeneous and Functionally Graded Materials (FGMs). The failure criterion is incorporated in the CZM using both a finite cohesive strength and work to fracture in the material description. A novel CZM for FGMs is explored and incorporated into a finite element framework. The material gradation is approximated at the element level using a graded element formulation. A numerical example is provided to demonstrate the efficacy of the CZM approach, in which the influence of the material gradation on the crack growth pattern is studied.

Keywords: Finite element method, functionally graded material (FGM), cohesive zone model (CZM), dynamics, crack, fracture.

INTRODUCTION

Fracture mechanics of Functionally Graded Materials (FGMs) has been an active area of research during recent years. Compared to the classical linear elastic fracture mechanics (LEFM) and some other existing fracture models, Cohesive Zone Models (CZMs) provide advantages of allowing spontaneous crack nucleation, branching, fragmentation and propagation without an external fracture criterion [1, 2].

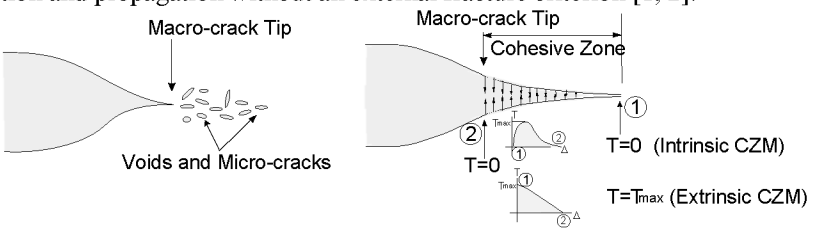

FIGURE 1. Schematic representation of cohesive zone model concept; (a) Material softening occurs around crack tip due to voids and micro-cracks; (b) CZM considers material softening and separation using distributed cohesive tractions along a cohesive surface at the crack tip vicinity. Circled numbers ① and ② denote the corresponding positions on the cohesive zone and cohesive law curves where material begins to soften (①) and where material completely loses fracture resistance capacity (②).

CP973, *Multiscale and Functionally Graded Materials 2006*
edited by G. H. Paulino, M.-J. Pindera, R. H. Dodds, Jr., F. A. Rochinha, E. V. Dave, and L. Chen

CZMs incorporate a cohesive strength and finite work to fracture in the description of material behavior, and allow simulation of near-tip behavior and crack propagation. The concept of "cohesive failure" is illustrated in Figure 1, in which a cohesive zone, along the plane of potential crack propagation, is present in front of the crack tip. Within the extent of the cohesive zone, the material points which were identical when the material was intact, separate to a distance Δ due to influence of high stress state at the crack tip vicinity. The cohesive zone surface sustains a distribution of tractions T which are function of the displacement jump across the surface Δ, and the relationship between the traction T and separation Δ is defined as the constitutive law for the cohesive zone surface.

CZMs can be categorized into two major groups: intrinsic CZMs and extrinsic CZMs. For intrinsic CZM as employed in this numerical example, the traction T first increases with increasing interfacial separation Δ, reaches a maximum value T_{max}, then decreases and finally vanishes at a characteristic separation value δ_n, where complete decohesion is assumed to occur. In this paper, a novel cohesive zone model developed for FGMs [3] is adopted to simulate dynamic crack growth in FGMs.

NUMERICAL SCHEME

To incorporate a CZM into the numerical scheme for dynamic fracture, the *cohesive element* is developed and positioned along the potential path or region of crack propagation, and attached to the volumetric elements, which follows a cohesive *traction-separation* relationship as shown in Figure 1. In contrast, the conventional finite element, which is now called "bulk element"', follows conventional *stress-strain* relationships (continuum description). The constitutive law of cohesive elements is inherently embedded in the finite element model, so that the presence of cohesive elements allows spontaneous crack propagation.

The FEM formulation incorporating cohesive elements is derived from the principle of virtual work, and discretized using the explicit central difference time stepping scheme to update displacements $\mathbf{u}$, accelerations $\ddot{\mathbf{u}}$ and velocities $\dot{\mathbf{u}}$ as follows:

$$\mathbf{u}_{n+1} = \mathbf{u}_n + \Delta t \dot{\mathbf{u}}_n + \tfrac{1}{2}(\Delta t)^2 \ddot{\mathbf{u}}_n \tag{1}$$

$$\ddot{\mathbf{u}}_{n+1} = \mathbf{M}^{-1}(\mathbf{F} - \mathbf{R}_{\text{int}(n+1)} + \mathbf{R}_{coh(n+1)}) \tag{2}$$

$$\dot{\mathbf{u}}_{n+1} = \dot{\mathbf{u}}_n + \tfrac{1}{2}\Delta t(\ddot{\mathbf{u}}_n + \ddot{\mathbf{u}}_{n+1}) \tag{3}$$

The symbols $\mathbf{M}$ denotes diagonal mass matrix, $\mathbf{F}$, $\mathbf{R}_{\text{int}}$ and $\mathbf{R}_{\text{coh}}$ denote external, internal and cohesive force vector, and Γ denotes domain boundary. To treat the material nonhomogeneity inherent in the problem, graded elements, which incorporate material property gradient at the element level, are introduced. In this investigation, the scheme proposed by Kim and Paulino [4] is adopted. The same shape functions are used to interpolate the unknown displacements, the geometry, and the material parameters, and thus the interpolations for material properties E, ν, ρ are given by

$$E = \sum_i^m N_i E_i, \quad \nu = \sum_i^m N_i \nu_i, \quad \rho = \sum_i^m N_i \rho_i \tag{4}$$

where N_i are the standard shape functions.

BILINEAR COHESIVE ZONE MODEL FOR FGMS

Insertion of cohesive elements introduces fictitious compliance to the structure, which is inherent to the "intrinsic" CZM approach. The magnitude of artificial compliance introduced is primarily related to the initial slope of the traction-separation law. A stiffer slope represents more rigid initial bonds between bulk elements, resulting in less fictitious compliance. A bilinear cohesive model [5,6] is thus adopted in favor of its adjustable slope attribute. It is assumed that the material fails when the parameter λ (a function of the normal and tangential separations) reaches unity:

$$\lambda = \sqrt{\left(\frac{\Delta_n^2}{\delta_n^2}\right) + \left(\frac{\Delta_t^2}{\delta_t^2}\right)} \tag{5}$$

The parameters Δ_n, Δ_t are the current normal and tangential cohesive interface separations, while δ_n, δ_t are the critical separation values at which the interface is considered to have failed in the two modes, respectively. The choice of a "critical separation" λ_{cr} allows the users to specify the initial slope of the cohesive law. The cohesive law is stated as

$$T_n = T_n^{\max}\frac{\Delta_n}{\delta_n}\frac{1-\lambda^*}{\lambda^*(1-\lambda)}, \qquad T_t = T_t^{\max}\frac{\Delta_t}{\delta_t}\frac{1-\lambda^*}{\lambda^*(1-\lambda)}, \qquad \lambda^* = \begin{cases}\lambda_{cr} & \text{if} \quad \lambda < \lambda_{cr} \\ \lambda & \text{if} \quad \lambda > \lambda_{cr}\end{cases} \tag{6}$$

The traction-separation relationships for pure mode I and pure mode II cases are plotted in Figure 2. Irreversibility of interface weakening is introduced by specifying

$$\lambda = \max(\lambda_{current}, \lambda_{previous}) \tag{7}$$

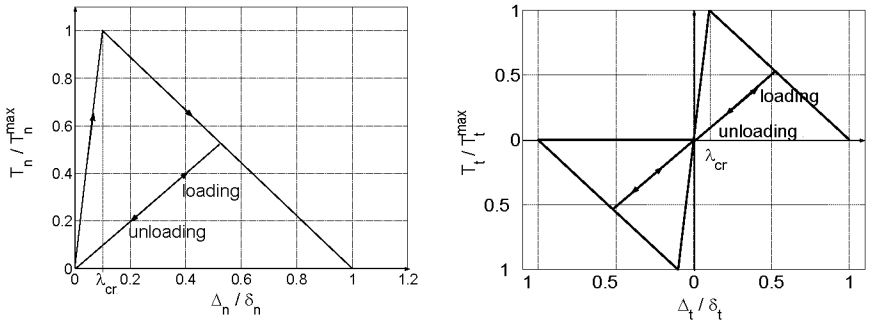

(a) (b)

FIGURE 2. Bilinear cohesive model for pure normal (a) and pure tangential (b) traction-separation.

In order to simulate crack propagation in FGM, we extended the bilinear model of Figure 2 to incorporate material gradation considerations. The cohesive traction force vectors associated with material phases 1 and 2 ($\mathbf{T}_1 = [T_{n1};\ T_{t1}]$; $\mathbf{T}_2 = [T_{n2};\ T_{t2}]$) are determined from Eqs. (5). The cohesive traction vector for a two-phase FGM ($\mathbf{T}_{FGM}$) is approximated by the volume fraction based formula

$$\mathbf{T}_n^{FGM}(x) = \frac{V_1(x)}{V_1(x)+\beta_1[1-V_1(x)]}\mathbf{T}_{n1}^{\max}\frac{\Delta_n}{\delta_{n1}}\frac{1-\lambda_1^*}{\lambda_1^*(1-\lambda_{cr1})} + \frac{1-V_1(x)}{1-V_1(x)+\beta_2 V_1(x)}\mathbf{T}_{n2}^{\max}\frac{\Delta_n}{\delta_{n2}}\frac{1-\lambda_2^*}{\lambda_2^*(1-\lambda_{cr2})} \tag{8}$$

$$\mathbf{T}_t^{FGM}(x) = \frac{V_1(x)}{V_1(x)+\beta_1[1-V_1(x)]}\mathbf{T}_{t1}^{\max}\frac{\Delta_t}{\delta_{t1}}\frac{1-\lambda_1^*}{\lambda_1^*(1-\lambda_{cr1})} + \frac{1-V_1(x)}{1-V_1(x)+\beta_2 V_1(x)}\mathbf{T}_{t2}^{\max}\frac{\Delta_t}{\delta_{t2}}\frac{1-\lambda_2^*}{\lambda_2^*(1-\lambda_{cr2})} \tag{9}$$

where the parameter $V_1(x)$ denotes volume fraction of the material phase 1, β_1 and β_2 denote two cohesive gradation parameters that describe the transition of failure mechanisms from pure material phase 1 to pure material phase 2.

MIXED-MODE DYNAMIC CRACK PROPAGATION

In this section, the cohesive zone model is employed to study a mixed-mode dynamic crack propagation problem, where the cohesive elements allow crack initiation and turning of crack paths to occur spontaneously without predefining crack path nor prescribing a separate fracture criterion.

Kalthoff-Winkler Experiments

Kalthoff and Winkler [7] tested specimens, as shown in Figure 3 (a), where a plate with two edge notches is subjected to an impact by a projectile. The experiments demonstrated different fracture/damage behaviors of a maraging steel material under various loading rates. The material properties are listed in Table 1. In this study, we only attempt to simulate the brittle failure mode and investigate the overall crack propagation angle, crack initiation time and propagation speed with a set of progressively refined element sizes. The impact loading rate is chosen as 16.5m/s. Since the problem possesses symmetry, only half of the geometry is modelled, as shown in Figure 3 (b).

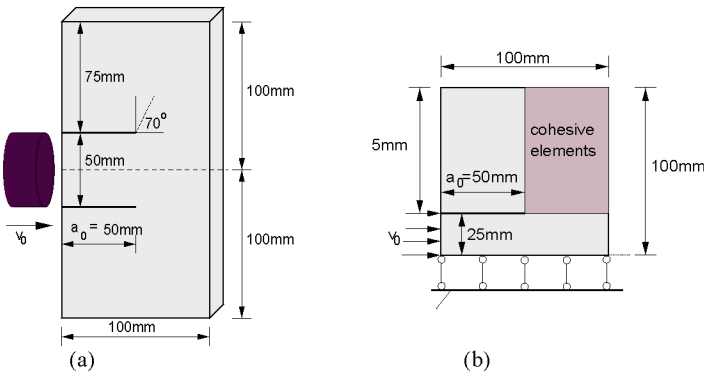

FIGURE 3. (a) Geometry and loading of the Kalthoff-Winkler experiments [7]; (b) 2-D plane-strain FEM simulation model.

The crack trajectory in this problem is not known a priori. In order to simulate crack propagation along arbitrary path, cohesive zone elements are inserted into a relatively large region through which the crack may potentially grow, as shown in Figure 3 (b).

TABLE 1. Material properties of 18Ni(300) steel and cohesive model parameters

E (GPa)	ν	ρ (kg/m^3)	G_{Ic}=G_{IIc} (kJ/m^2)	T_n^{max}=T_t^{max} (GPa)	δ_n=δ_t (μm)
190	0.3	8000	22.2	1.733	25.63

Homogeneous Material Results

Two sets of calculations are carried out to investigate the capabilities of the bilinear cohesive model. The first set aims to study the effect of mesh orientation on the fracture propagating path. Three rectangular unit cells with aspect ratios of height/width = {25/16, 1, 16/25} are considered. Therefore, the plate geometry is discretized into 64×100, 80×80 and 100×64 rectangles, each divided into 4 T6 elements. The second set of calculations investigates the effect of mesh size. Results obtained from 100×100 and 120×120 are compared to that from 80×80, for instance.

Initially, all bulk elements are bound together with cohesive force provided by the cohesive elements. Fracture occurs at high stress regions, where the local stress overcomes cohesive strength and the cohesive elements gradually lose resistance capability against separation, as shown in Figure 4.

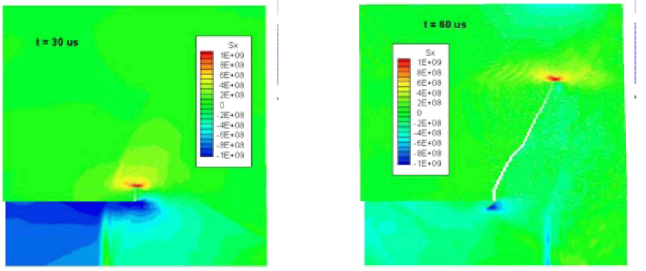

(a) (b)

FIGURE 4. Stress field σ_x and crack evolution in a 120×120 grid mesh; (a) crack pattern at t = 30μs; (b) crack pattern at t = 60 μs.

The fracture paths for three aspect ratios of the "unit mesh grid" are shown in Figure 5 (a). Despite the different mesh orientation bias, the overall crack propagation paths of the three different meshes are similar. The propagation angle is estimated to be around 72° to 74°, which agrees well with the experimental prediction (70°). Further refined mesh results are shown in in Figure 5 (b) for mesh with aspect ratio of 1, which indicate similar crack pattern, especially before crack approaches boundary.

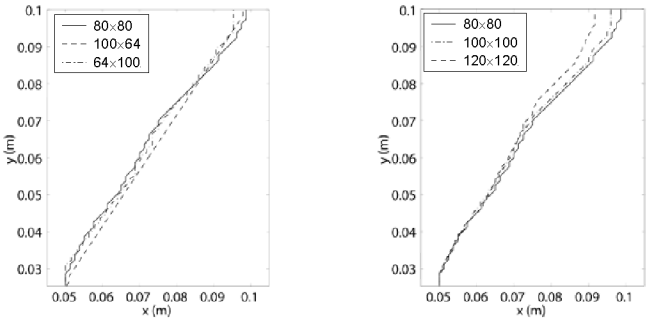

(a) (b)

FIGURE 5. (a) Influence of mesh discretization on dynamic fracture behavior; (a) final crack paths for the first set of mesh discretization with total number of 25,600 T6 elements, and different mesh orientations; (b) final crack paths for square shape grids with element sizes h = 1.25,1, 0.8mm.

Graded Material Results

Consider linearly graded Young's modulus E, fracture toughness G and cohesive strength T_n^{max} along the Cartesian x direction, as shown in Table 2.

TABLE 2. Graded Material properties

Material	E_1 (GPa)	E_2 (GPa)	G_1 (kJ/m^2)	G_2 (kJ/m^2)	T_1^{max} (GPa)	T_2^{max} (GPa)	t_{init} (μs)
Homogenous	190	190	22.2	22.2	1.733	1.733	20.7
FGM-LHS softer	127	253	14.8	29.6	1.155	2.301	24.8
FGM-RHS softer	253	127	29.6	14.8	2.301	1.155	18.2

The crack paths are plotted in Figure 6 for the graded specimens as well as the homogeneous case. Apparently, the crack tends to grow into the weaker region. After the velocity loading is applied to the lower left surface, the stress waves propagate rightwards and the stress concentration builds up at the crack tip. Since the material fracture toughness at the initial crack tip are the same for all three cases, the crack initiation time is primarily determined by the rate of stress concentration at the crack tip. Because the material stiffness varies along the x direction, the stress waves propagate at varying speeds. For the "RHS softer" specimen, the average stiffness between the left surface and the crack tip is higher than the other two cases, and consequently the average wave speed is faster. Therefore, it takes shorter time for the crack tip tensile stress to reach the critical value for this case than the opposite material gradation case, and thus the crack initiates earlier.

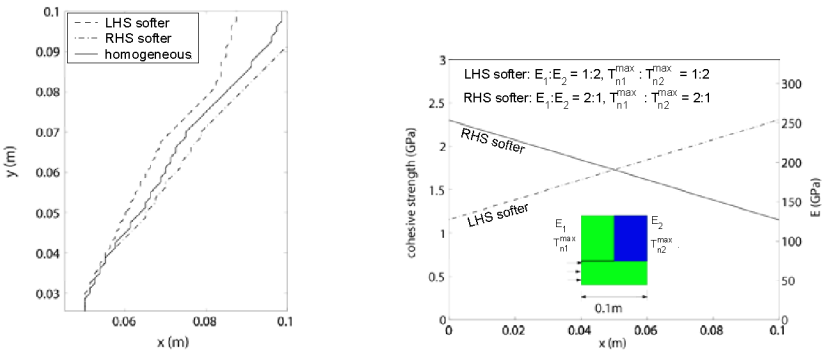

(a) (b)

FIGURE 6. (a) Comparison of fracture paths for graded stiffness and graded fracture toughness along the Cartesian x direction. (b) material gradation profiles for E and cohesive strength.

REFERENCES

1. X. Xu and A. Needleman, *International Journal of Fracture*, **74**, 289-324 (1995).
2. M. Ortiz and A. Pandolfi, *International Journal for Numerical Methods in Engineering*, **44**, 1267-1282 (1999).
3. Z. Zhang and G. H. Paulino, *International Journal of Plasticity*, **21**, 1195-1254 (2005)
4. J-. H. Kim and G. H. Paulino, *ASME Journal of Applied Mechanics*, **69**, 502-514 (2002).
5. P. H Geubelle and J. Baylor. *Composites Part B Engineering*, **29**, 589-602 (1998)
6. P. Zavattieri and H. Espinosa, *Acta Mater.*, **49**, 4291-4311 (2001).
7. J. F. Kalthoff and S. Winkler, *International Conference on Impact Loading and Dynamic Behavior of Materials*, Edited by C. Y. Chiem, H.D. Kunze and L. W. Meye, pp. 185-195, 1987.